The Interaction Between the ISO Tapping Machine and Lightweight Floors

Jonas Brunskog, Per Hammer

The Interaction Between the ISO Tapping Machine and Lightweight Floors

Jonas Brunskog, Per Hammer
Division of Engineering Acoustics, LTH, Lund University, Sweden. Jonas.Brunskog@acoustics.lth.se

The ISO standard tapping machine, used as an excitation source in rating the impact-sound level of a floor structure, interacts with the floor structure during the hammer impact. Expressions for the force spectrum due to the impact are presented. The 6 dB difference at low frequencies of the force spectrum, evident in measurements, and reasons for it, are discussed. The interaction is investigated by use both of simplified lumped models and arbitrary frequency-dependent models. Local effects due to indentation near the point of impact and to global effects due to stiffeners are included in the description of the mobility involved. Numerical results are presented, where it is concluded that both the local and the global effects of the driving-point mobility are important in describing the force spectrum caused by the interaction between the tapping machine and the complex floor structure.

1. Introduction

The use of lightweight building techniques has increased during the last few years. It is well-known, however, that structures of this type often have poor impact-sound insulation. A prediction model is an important tool in developing structures that have acceptable insulation characteristics and in explaining how they function. A model for predicting impact noise can be said to consist of three parts: the excitation, the system and the response. The present paper focuses on the excitation part. Point impact excitation can be caused by e.g. footsteps or the impact of dropped items. Excitation can also be produsedby the ISO standard tapping machine [1], as dealt with in the present paper. Thus, the paper aims at deriving expressions for the force spectrum produced by the impact of a hammer on a lightweight floor.

The system, or more specifically the representation of the floor system in question, is important not only as a transfer part from excitation to response, but also of deriving the impact force. It is important, therefore, that attention be directed at the interaction between the hammer and the floor. The system and the response are examined in greater detail in [2], in which measurements are also compared with predictions derived from a model. A comprehensive survey of the literature on prediction model approaches is presented in [3].

The ISO standard tapping machine can be used as an excitation source for rating the impact-sound level of a floor structure. Although the machine provides no genuine simulation of real footsteps, the test results obtained yield valuable information concerning the dynamic behaviour of the floor. If the description of the tapping machine as a source is sufficiently thorough and precise, it may be possible sometime in the future to solve the problem of the correlation between sound disturbances by footsteps and the impact sound level produced by the machine.

Cremer has derived the impact noise level caused by a tapping machine for homogenous structures of high impedance, the results being summarised by Cremer and Heckl [4, pp. 269–271, 333–339]. In dealing with a bare slab Cremer makes use of momentum calculations that assume there to be a perfect elastic impact (described in section 2 of the present paper) the results are quit satisfactory. However, when taking into account the effects of a resilient floor covering, Cremer's description of the problem implies that the hammer becomes stuck to the floor after impact. This leads to resonant behaviour that is not to be found in measurements according to the ISO standard. In fact, the hammer rebounds after impact, there being only an initial positive force pulse present, a matter investigated by Lindblad [5]. Also, regarding linear excitation Lindblad considered the effect of an energy-consuming part of the deformation, conceived as a resistance in series with a spring to represent the resilient covering. The resistance can be due to local material damping or, as in the present study, to energy being transported within the plate away from the region of impact. For heavy slabs, as considered in references [4, 5, 6], the resilient part is due to the floor covering. Lindblad's major interest, however, was in the non-linear behaviour of coverings that interact with the hammer. Vér [6] derived a complete and accurate descrip-

tion of the force spectrum and the impact noise level a tapping machine produces on hard surfaces, including the rebound. The improvement in insulation achieved by use of an elastic surface layer (floor covering) or of floating floors with surfaces of high impedance is also considered.

A lightweight floor structure can usually not be regarded as a homogenous structure of high impedance. It consists of thin plates of wood, chipboard, gypsum, or whatever, and is reinforced by joist stiffeners. Thus, it cannot be assumed that the force spectrum in [4, 5, 6] is applicable generally. Nevertheless, in more recent papers on impact-sound insulation, such as Gerretsen [7], the momentum model of Cremer and Heckl [4] has continued to be used, also for non-homogenous or lightweight floors. Thus, it is common to assume the force spectrum to be invariant with respect to the excitation system (i.e. of its being a linear source with infinite source mobility). In the present paper no such assumption is made. In another recent paper, by Scholl et al. [8], the interaction between the source, the floor covering and the floor structure is considered. However, the floor structure is represented by the mass of the structure, not taking into account that the driving-point impedance of a plate on average has the characteristics of a resistance (i.e. $8\sqrt{m''B}$), and in general is complex. Thus, no energy (or momentum) consuming part is included in the model used by Scholl.

Measurements, such as those of Hall's [9], indicates there to be a 6 dB gap at low frequencies between the force (or acceleration) spectrum of a hammer impacting on a high impedance surface such as concrete and its impacting on a low impedance surface such as an mdf-board. This can easily be explained in terms of simple momentum consideration in a manner comparable with the case to which Cremer's [4] calculations but letting the hammer be stuck to the plate, as will be taken up in section 2.

The organisation of the paper is as follows: In order to obtain a force spectrum of a form suitable for the solution technique applied to the system described in [2], the findings reported in [4, 5, 6] are integrated and reanalysed in sections 2 and 3, several numerical examples being provided there. A system of arbitrary frequency-dependent driving-point mobilities is then added in section 4, in which different causes for the frequency-dependent driving-point mobilities are discussed. The procedure for evaluating these mobilities numerically is described in section 5. The numerical results are presented in section 6, the conclusions being summarized, finally, in section 7.

The present analysis is based on linear theory implying that the contact area during impact is constant, as discussed in section 3.2. The displacement of the receiver structure is in addition small, and therefore assumed to be within the linear range. It should be noted, however, that a direct linear-system analysis is not applicable since the system is changed when the object producing the impact leaves the structure with which it has had contact. Thus, the boundary condition between the object and the structure is rather being an inequality than an equation, and the situation is not time-invariant.

2. The hammer impact force in the time and the frequency domain

The ISO standard tapping machine [1] consists of five hammers spaced equally along a line 40 cm in length. As an approximation, it is assumed here, however, that all hammer impacts act on the same position. Each hammer has a mass of $M = 0.5$ kg and it is dropped from a height h of 4 cm. The hammers strike the floor with a rate of $f_r = 10$ times per second, giving a repetition time of $T_r = 1/f_r = 0.1$ s. Consider initially, however, a single hammer impact with the force time history $f_1(t)$. The Fourier spectrum of this force pulse is $F_1(f) = \mathcal{F}_t\{f_1(t)\}$, $\mathcal{F}_t\{\cdot\}$ being the Fourier transform operator (time to frequency). In the present paper, the word spectrum is used to denote a function in the (Fourier) frequency domain. The excitation caused by the tapping machine can be regarded as an array of separate force pulses $f_1(t)$. The time history of the repeated force $f_R(t)$ is thus

$$f_R(t) = \sum_{n=-\infty}^{\infty} f_1(t - nT_r). \tag{1}$$

This time history is a periodic signal. Accordingly, it can be represented by a Fourier series, e.g. by the two-sided complex Fourier series

$$f_R(t) = \sum_{n=-\infty}^{\infty} F_n \mathrm{e}^{\mathrm{i}2\pi nt/T_r}. \tag{2}$$

The signal is represented by a Fourier series consisting of an infinite number of discrete frequency components of amplitude F_n. The Fourier spectrum for the signal is the tonal spectrum

$$F_R(f) = \mathcal{F}_t\{f_R(t)\} = \sum_{n=-\infty}^{\infty} F_n \delta(f - nf_r) \tag{3}$$

where $F_R(f)$ denotes the spectrum of the repeated signal. It was used in [2] as the excitation force of the system, whereas δ denotes the Dirac delta function. Each amplitude is given by

$$F_n = \frac{1}{T_r} \int_0^{T_r} f_1(t) \mathrm{e}^{-\mathrm{i}2\pi nt/T_r} \mathrm{d}t \tag{4}$$

where, as indicated above, $f_1(t)$ is the force time history of a single hammer impact. This integral is identical with the Fourier transform of the individual force pulse except for the factor $1/T_r$. Thus, for the tapping machine the repeated force components F_n is 10 s^{-1} times the force spectrum for a single impact. If a trigonometric Fourier series is used instead, each sine or cosine component is twice that in (4). This is due to the two-sided representation described in (2), which is the most suitable representation in the present situation, since the force spectrum is used in a two-sided model, i.e. one in which there is assumed to be an $\mathrm{e}^{\mathrm{i}wt}$ dependence. Cremer [4] and Vér [6] used a one-sided rep-

resentation, together with a RMS and a (third) octave band procedure.

For low-frequency components the force pulse is usually short compared with the period of interest. Accordingly, the Fourier amplitude of the force pulse train during the effective interval of the force pulse, $\exp(-\mathrm{i}2\pi nt/T_r) \approx 1$, can be approximated by

$$F_n|_{f\to 0} = \frac{1}{T_r}\int_0^{T_r} f_1(t)\mathrm{d}t \tag{5}$$

which is the mechanical impulse divided by T_r, the mechanical impulse being equal to the change in momentum. The hammer hits the slab with a velocity $v_0 = (2gh)^{1/2} = 0.886$ m/s. If the impact is purely elastic, the momentum of the hammer after impact is equal in magnitude to that prior to impact but is of the opposite sign, the hammer lifting from the slab with the velocity v_0. Thus, $F_n|_{f\to 0} = 2Mv_0/T_r = 8.859$ N (where for a single force pulse the corresponding low-frequency asymptote is $F_1|_{f\to 0} = 2Mv_0$). Since this is the highest possible low-frequency asymptote of the impact spectrum, it is the maximum value for the magnitude of the spectrum. At the other extreme, if the impact is so damped that the entire momentum is dissipated during impact, the hammer does not rebound. The mechanical impulse is then $F_n|_{f\to 0} = Mv_0/T_r = 4.430$ N ($F_1|_{f\to 0} = Mv_0$). This is the lowest possible low-frequency asymptote of the impact spectrum. Thus, these two cases constitute the upper and lower bounds of the low-frequency asymptote of the force spectrum, which represents a span of 4.429 N, or 6 dB. As indicated above, this span can be clearly seen in measurements that have been made [9].

3. Impact force and lumped system

In order to include cases between the two extremes just referred to, a lumped model can be employed, one that provides a somewhat more realistic description than that of momentum consideration does. The model and the solution arrived at are taken from Lindblad [5], whereas the physical situation and the analysis are new. A treatment of general frequency-dependent impedances is found in section 4.

3.1. A single slab, interaction between hammer and floor

A lumped model of the impact of the hammer on a single slab floor is shown in Figure 1. The floor consists of a resilient part and an energy consuming part, represented by a spring with stiffness K and by a dashpot with resistance R, respectively. The physical meaning of the two components is discussed in section 3.2.

When the hammer has reached the slab, the differential equation for the system assumed is

$$\begin{aligned} M\partial^2\xi_K/\partial t^2 &= K(\xi_K - \xi_R) \\ K(\xi_R - \xi_K) &= R\partial\xi_R/\partial t \end{aligned} \tag{6}$$

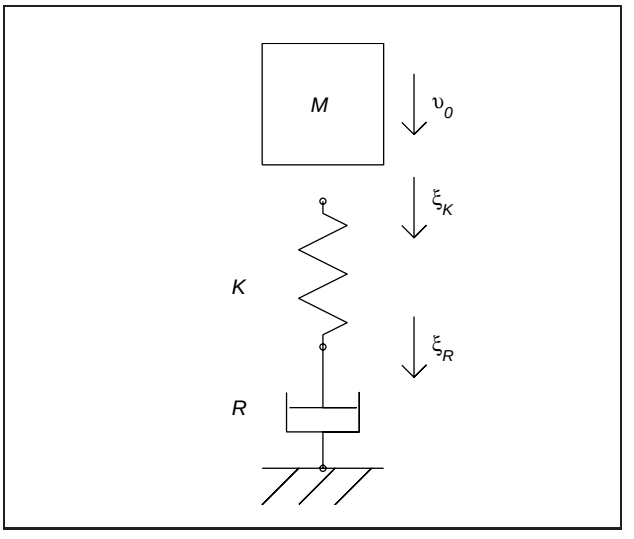

Figure 1. Model of hammer impact.

where ξ_K and ξ_R are displacements. Under the initial condition v_0, and assuming frequency independent K and R, the solution is found to be [5]

$$f_1(t) = \begin{cases} v_0 K \frac{\sinh(\Omega_{oc}t)}{\Omega_{oc}}\mathrm{e}^{-Kt/2R}, & KM \geq 4R^2 \\ v_0 K \frac{\sin(\Omega_{uc}t)}{\Omega_{uc}}\mathrm{e}^{-Kt/2R}, & KM < 4R^2 \end{cases} \tag{7}$$

which of these applies depending on whether the oscillation is overcritical or not, where

$$\begin{aligned} \Omega_{oc} &= \sqrt{(K/2R)^2 - K/M} \\ \Omega_{uc} &= \sqrt{K/M - (K/2R)^2} \end{aligned}$$

are the overcritical and the undercritical angular frequency, respectively. In Lindblad [5] the first of these is denoted as the 'stuck to the floor' case and the latter as the 'rebound' case. If an overcritical oscillation is present, a numerically more appropriate form would be to write the expression in terms of exponential functions instead of hyperbolics combined with exponentials. For $R \to \infty$, or if $\xi_R = 0$, equation (7) is replaced by

$$f_1(t) = v_0 K \sin(\sqrt{K/M}t)/\sqrt{K/M} \tag{8}$$

which is an undamped oscillation in which $f_{cut}^{ud} = 1/(2\pi)(K/M)^{1/2}$ is the undamped natural frequency (and cutoff frequency). The force starts at zero at the moment the hammer hits the slab, and increases to a maximum, at which point the hammer reaches its maximum depth, the hammer then starting to return and the force decreasing. As the force reaches the zero crossing at $t_{cut} = 1/(2f_{cut})$, the hammer rebounds, takes off from the slab and is picked up by a catching mechanism (an eccentric cam). Thus, the force is zero after this moment,

$$f_1(t) = \begin{cases} \frac{v_0 K}{\sqrt{K/M}}\sin(\sqrt{K/M}t), & 0 < t < \frac{1}{2f_{cut}} \\ 0, & \text{else.} \end{cases}$$

The same conditions hold for the damped oscillations described in (7). In the overcritical case the force will never completely be zero. However, the force still decreases rapidly after reaching the maximum and is approximately zero at T_r. Each amplitude in the tonal spectrum of the ISO tapping machine is given then by

$$F_n = \frac{1}{T_r}\int_0^{T_r \approx \infty} f_1(t)\mathrm{e}^{-\mathrm{i}2\pi nt/T_r}\,\mathrm{d}t \tag{9}$$

in the case of overcritical damping, and by

$$F_n = \frac{1}{T_r}\int_0^{t_{cut}} f_1(t)\mathrm{e}^{-\mathrm{i}2\pi nt/T_r}\,\mathrm{d}t \tag{10}$$

in the case of undercritical damping. These integrals can be expressed in closed form, but are likewise well suited for numerical integration. The Fourier transforms of a single impact are given below, where the cutoff frequencies are also determined. For the over-critical case, the inequality $K/2R > \Omega_{oc}$ holds, giving a Fourier transform over time to angular frequency $\omega = 2\pi f$ of equation (7),

$$\begin{aligned} F_{1,oc} &= \mathcal{F}_t\{f_1(t)|_{oc}\theta(t)\} \\ &= \frac{v_0 KM}{K - \omega^2 M + \mathrm{i}\omega KM/R} \end{aligned} \tag{11}$$

where $\theta(t)$ is the unit step function. The low-frequency asymptote of (11) is

$$F_{1,oc}|_{f\to 0} = v_0 M$$

as expected. In the undercritical case, a Fourier transform over time of equation (7) yields, taking into account the time interval of interest

$$\begin{aligned} F_{1,uc} &= \mathcal{F}_t\{f_1(t)|_{uc}\big(\theta(t) - \theta(t - t_{cut})\big)\} \\ &= \frac{v_0 KM\left(1 + \mathrm{e}^{-t_{cut}(\mathrm{i}\omega + K/2R)}\right)}{K - \omega^2 M + \mathrm{i}\omega KM/R} \end{aligned} \tag{12}$$

where

$$t_{cut} = \pi/\Omega_{uc} = 1/2f_{cut}$$

is the time of zero-crossing. The low-frequency asymptote is

$$F_{1,uc}|_{f\to 0} = v_0 M\left(1 + \mathrm{e}^{-Kt_{cut}/2R}\right)$$

which has two extremes depending on the resistance R,

$$F_{1,uc} = \begin{cases} 2v_0 M, & f \to 0 \text{ and } R \to \infty \\ v_0 M, & f \to 0 \text{ and } R \to \frac{1}{2}\sqrt{KM} \end{cases}$$

which agrees with the asymptotes schematically derived in section 2 on the basis of the mechanical impulse and the change in momentum.

In both the overcritical and the undercritical case, the Fourier series components are then found to be $F_n = F_1(nf_r)f_r$, and the complex cutoff angular frequency (i.e. the poles) is

$$\omega_{cut} = \mathrm{i}K/2R \pm \sqrt{K/M - K^2/(2R)^2} \tag{13}$$

If the negative sign is chosen, the absolute value of the complex cutoff angular frequency yields the point of interest on the real axis,

$$|\omega_{cut}| = \begin{cases} \frac{K}{2R} - \sqrt{\frac{K^2}{(2R)^2} - \frac{K}{M}}, & KM \geq 4R^2 \\ \sqrt{\frac{K}{M}}, & KM < 4R^2 \end{cases} \tag{14}$$

The cutoff frequency then is

$$f_{cut} = |\omega_{cut}|/2\pi, \tag{15a}$$

whereas in the undercritical case the undamped cutoff frequency,

$$f_{cut}^{ud} = 1/(2\pi)\sqrt{K/M} \tag{15b}$$

is employed, this being the frequency at which the phase equals $-\pi/2$.

3.2. Choice of the frequency independent stiffness and resistance

In Figure 1 the impedance at the position where the hammer hits the floor is represented by a spring and a dashpot in series. Thus, a suitable stiffness K and a resistance R need to be found in order to achieve an adequate approximation of what occurs at impact. The resilient part is often the result of there being an elastic surface layer on an otherwise bending stiff slab. The stiffness of the elastic layer is then $K = EA_h/d$, c.f. Vér [6], where E is Young's modulus, d is the thickness of the elastic layer, and A_h is the area of the hammer. The resistance is then related to the local dissipation, $R = \eta(KM)^{1/2}$, η being the loss factor for the material. In the lightweight floor structures considered in this paper, however, the hammer hits a rather thin plate made of gypsum or of wooden material. It can thus be assumed that the resilient part is due to local deformation of the plate, and the resistive part to energy transportation within the plate. As a first approximation, the stiffness of the local deformation can be found, as in [10, 11], by

$$K = 2GD_h/(1-\nu) = ED_h/(1-\nu^2) \tag{16}$$

where G is the shear modulus, ν is Poisson's ratio and $D_h = 2(A_h/\pi)^{1/2}$ is the diameter of the hammer. The local stiffness here is found for a static deformation caused by a rigid stamp on a semi-infinite elastic solid, the so-called Bossinesq deformation. If the area of contact between the hammer and the floor can be regarded as involving contact between two elastic bodies of different radii, a geometric non-linearity will occur, a so-called Hertz deformation [10]. The hammers of the tapping machine are actually not entirely flat, but since after a few impacts the material in the impact zone becomes somewhat plastically

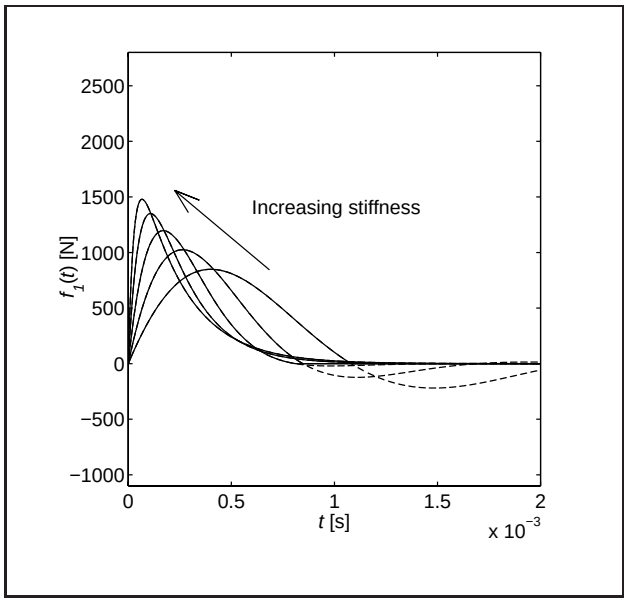

Figure 2. Time history of hammer impact. Solid line (—) denotes the interrupted force, dashed line (- - -) denotes the oscillating force. The parameters are $K = \{5\ 10\ 20\ 40\ 80\} \cdot 10^6$ N/m, $R = 2 \cdot 10^3$ Ns/m.

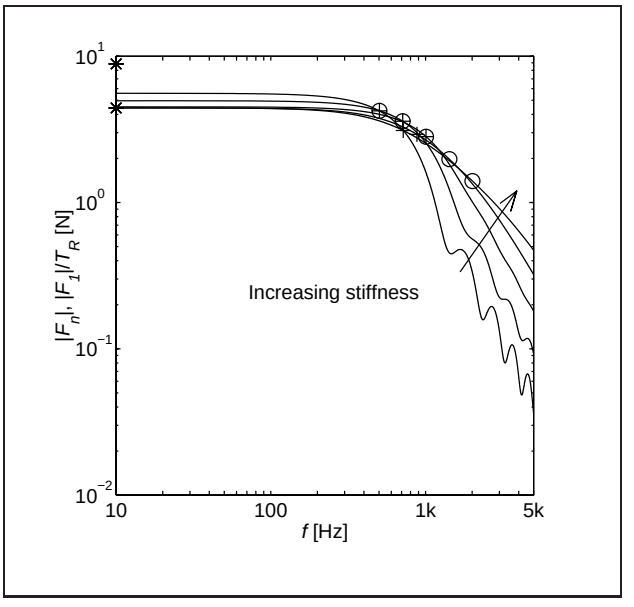

Figure 3. Hammer impact spectrum, showing magnitudes. The parameters are $K = \{5\ 10\ 20\ 40\ 80\} \cdot 10^6$ N/m and $R = 2 \cdot 10^3$ Ns/m.

deformed by the hammer it is assumed that the Hertz deformation effect will not be dominant in the steady-state vibrational phase.

The resistance is taken to be the real driving-point impedance of a thin plate,

$$R = 8\sqrt{m'' B}, \tag{17}$$

its being taken into account that energy is transported away from the excitation point by bending wave motion. Here m'' is the mass per unit area and $B = EI'$ is the bending stiffness of the plate.

Both of these lumped parameters are frequency independent, a necessary condition for the solution technique described in section 3.1.

3.3. Numerical examples

Various numerical examples will be presented now to illustrate certain features of the lumped two-parameter description of the impact force of the tapping machine. The examples will come from a specific combination of R and K, where $R = 2 \cdot 10^3$ Ns/m and $K = 4 \cdot 10^6$ N/m. These values correspond roughly to an infinite 22 mm thick wooden plate, use being made of equations (16) and (17), respectively. The parameters are varied one at the time.

In Figures 2 to 4 the stiffness is varied as $K = \{5\ 10\ 20\ 40\ 80\} \cdot 10^6$ N/m. Figure 2 shows the time history of the impact force. The first three impact forces are undercritical, as indicated by the dashed line (- - -), since they should oscillate if uninterrupted. The increase in stiffness results in a narrower pulse, and thus a somewhat broader frequency range, as can be seen in Figure 3.

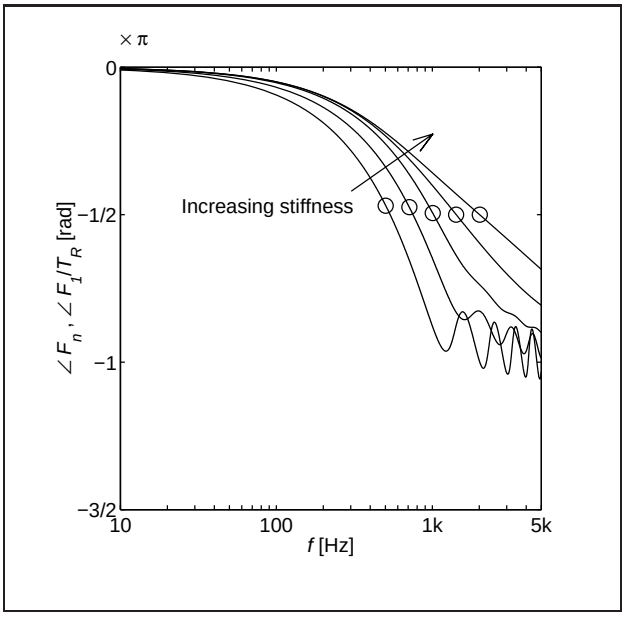

Figure 4. Hammer impact spectrum, showing the phases. The parameters are $K = \{5\ 10\ 20\ 40\ 80\} \cdot 10^6$ N/m and $R = 2 \cdot 10^3$ Ns/m.

Figure 3 shows the magnitude of the force spectrum, as derived from equation (11) or (12). The undamped cutoff frequency (15b) is indicated by circles (o) and the actual cutoff frequency (15a) by pluses (+). The extremes of the low-frequency asymptotes are indicated by two stars on the ordinata ($*$). The undercritical behaviour of the first three pulses manifests itself as oscillation in the high-frequency range. The overcritical force pulses are close to the lower extreme of the low-frequency asymptotes.

The behaviour of the cutoff frequency when the stiffness increases can be described as follows: The cutoff

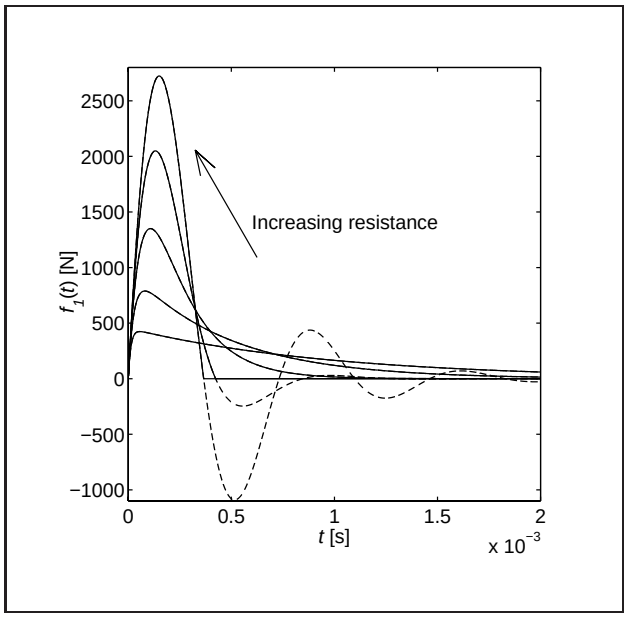

Figure 5. Hammer impact time history. Solid line (—) denotes the interrupted force, dashed line (- - -) denotes the oscillating force. The parameters are $R = \{0.5\ 1\ 2\ 4\ 8\} \cdot 10^3$ Ns/m and $K = 40 \cdot 10^6$ N/m.

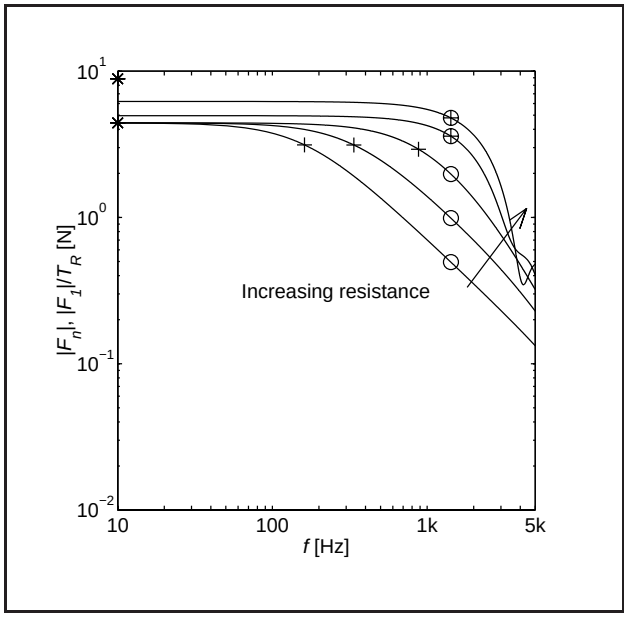

Figure 6. Hammer impact spectrum: magnitudes. The parameters are $R = \{0.5\ 1\ 2\ 4\ 8\} \cdot 10^3$ Ns/m and $K = 40 \cdot 10^6$ N/m.

frequency increases with increasing stiffness up to the point where critical damping occurs, where $K = 4R^2/M$. Thereafter the cutoff frequency decreases as the stiffness increases further. The undamped cutoff frequency always increases with increasing stiffness.

Figure 4 shows the phase of the force spectrum. The undamped cutoff frequency (15b) is marked by circles (o). As a reference to the phases, the time of impact is taken, giving a low-frequency asymptote of zero.

In Figure 5 to 7 the resistance is varied as $R = \{0.5\ 1\ 2\ 4\ 8\} \cdot 10^3$ Ns/m. Figure 5 shows the time history

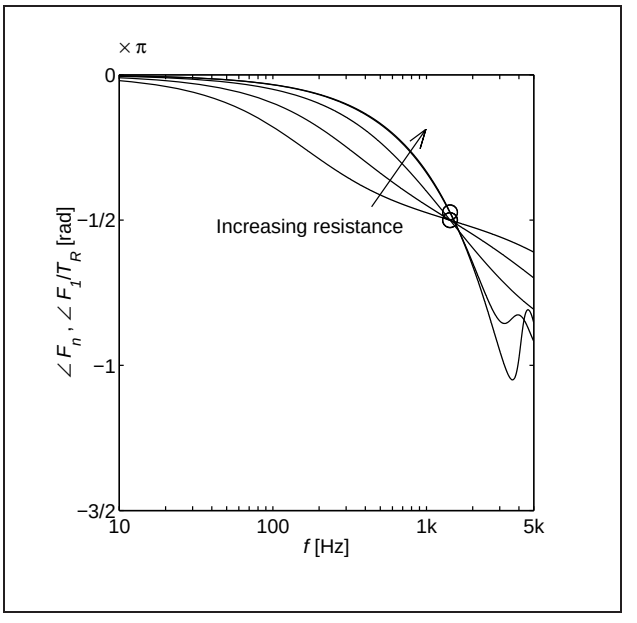

Figure 7. Hammer impact spectrum: phases. The parameters are $R = \{0.5\ 1\ 2\ 4\ 8\} \cdot 10^3$ Ns/m and $K = 40 \cdot 10^6$ N/m.

of the impact force. The two final impact forces are undercritical. The dashed line (- - -) indicates how they would have continued if uninterrupted. An increase in resistance results in the pulse becoming narrower, and thus in the frequency range becoming somewhat broader, as can be seen in Figure 6. The undamped cutoff frequency remains unchanged, however.

Figure 6 displays the magnitude of the force spectrum, as derived from equation (11) or (12). The undamped cutoff frequency (15b) is indicated by circles (o) and the actual cutoff frequency (15a) by pluses (+). The extremes of the low-frequency asymptote are indicated by two stars on the ordinata ($*$). The last spectrum ($R = 8 \cdot 10^3$ Ns/m) is not much affected by dissipation, the low-frequency asymptote consequently having increased. For the overcritical pulses, the spectrum starts to decrease at the actual (lower) cutoff frequency, not at the undamped one.

Figure 7 shows the phase of the force spectrum involved. The reference to the phases is taken at the time of impact, giving a low-frequency asymptote of zero. The undamped cutoff frequency (15b) is indicated by circles (o).

To conclude: increasing the stiffness gives a lower low-frequency asymptote and a higher cutoff frequency, whereas increasing the resistance gives a higher low-frequency asymptote and an unchanged undamped cutoff frequency (15b) and a lower actual cutoff frequency (15a).

3.4. Floating floors, a discussion

A floating floor can be described with two infinite plates connected by a resilient layer [4, 12]. To simplify the situation, it can be assumed that the plates are thin and that the resilient layer is point-reacting and massless. To simplify the situation still further, two different cases can be distinguished such that in the first case the impedance of

the excited plate is so high that the impact situation is the same as described in section 3.1–3.2, whereas in the second case the impedance of the excited plate is so low that the secondary (non-excited) plate can be regarded as rigid. In this second case the plate system can be simplified to a Winkler foundation, involving a plate resting on a locally reacting resilient layer. The bending wave-number is $k_B^4 = (m''\omega^2 - K)/B$, where m'' is the mass per unit area of the plate, K is the stiffness of the foundation and B is the bending stiffness of the plate. The driving-point mobility then is

$$Y = \frac{\omega}{-8B^{1/2}\mathrm{i}\sqrt{K - m''\omega^2}},$$

where the square-root in the denominator yield as a consequence that no lumped model can be used, even for this simple case. Thus, a more general description is needed.

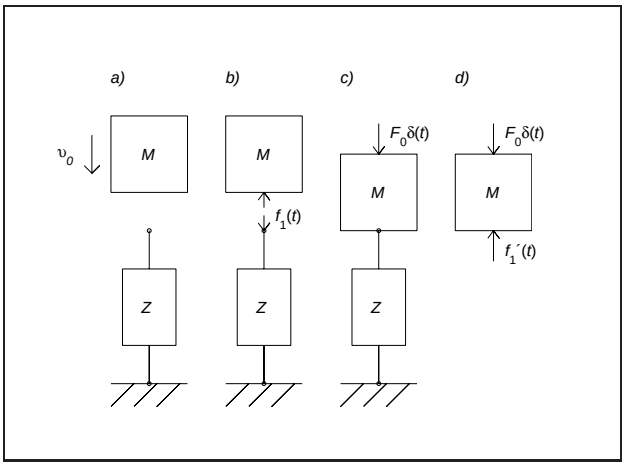

Figure 8. Modified impact description, impedance $Z = 1/Y$.

4. Impact force and the general system

In section 3 the impact force spectrum was derived for frequency-independent parameters K and R in a mechanical series. The spectrum was given explicit expressions (11–12). However, the floor system cannot generally be described in terms of frequency-independent parameters. The lumped description of the driving-point impedance/mobility is basically an ad hoc approximation of the actual situation. A more accurate description would be to calculate the driving-point mobility from the system description. The driving-point mobility is defined as the complex ratio of velocity to applied force, where the velocity is measured at the point of application of the force, c.f. [13].

Since the methods employed in section 3 cannot be used for frequency-dependent mobility, however, an approach to finding the force spectrum for an arbitrary driving-point mobility needs to be found. A suitable approach is to solve the differential equations in the frequency domain, inverse transform the result obtained in order to find the time of rebound, and to then transform the remaining force into the frequency range.

4.1. The interaction between the hammer and the floor

Figure 8 shows the generalised impact situation and the procedure employed. Figure 8 a) presents a general model of the impact. The hammer, of mass M, strikes the floor with the velocity v_0. The floor can be described in terms of the general driving-point mobility Y (or impedance $Z = 1/Y$). The desired force, $f_1(t)$, is shown in Figure 8 b).

The mobility is frequency-dependent, implying that the equations of motion can easily be solved in the frequency domain. On the other hand, the impact history is interrupted after the first zero crossing of the force. Thus the system is not time-invariant and therefore is best treated in the time domain. To deal with this problem, consider Figure 8 c), in which the mass M is now fixed on top of the impedance Z. The entire system is driven by a force $F_0\delta(t)$. This modified form of the problem is both linear and time-invariant. The equation of motion and the floor reaction force, if taken in the frequency domain, are

$$F_0 - F_1' = \mathrm{i}\omega M v,\ F_1' = v/Y, \tag{18}$$

where $v = \mathcal{F}_t\{v(t)\}$ is the velocity spectrum of the floor and F_1' is the spectrum of the continuing impact force, i.e. the floor reaction force between the mass and the impedance, as shown in Figure 8 c-d), $F_1' = \mathcal{F}_t\{f_1'(t)\}$. One solves then for F_1' and v,

$$F_1' = F_0/(1 + \mathrm{i}\omega MY), \tag{19a}$$

$$v = YF_1'. \tag{19b}$$

The magnitude of the force F_0 needs to be selected so that the velocity at $t = 0_+$ equals the velocity of the falling hammer. At $t = 0_-$ the velocity should be zero,

$$v(0_+) = v_0,\ v(0_-) = 0. \tag{20}$$

In evaluating $v(0)$, however, account needs to be taken of the fact that the Dirac $\delta(t)$ that excites the floor at time $t = 0$ is only at half inside the infinitesimal region from $t = 0$ to $t = 0_+$. This is compensated for if a value halfway between $v(0_+)$ and $v(0_-)$ is employed,

$$v(0)|_{Dirac} = v_0/2. \tag{21}$$

The velocity of the floor at $t = 0$ is evaluated as the integral over all the frequencies,

$$\begin{aligned} v(0) &= \frac{1}{2\pi}\int_{-\infty}^{\infty} v(\omega)\mathrm{d}\omega \\ &= \frac{F_0}{2\pi}\int_{-\infty}^{\infty} \frac{\mathrm{d}\omega}{\mathrm{i}\omega M + 1/Y(\omega)} \equiv F_0 I_0, \end{aligned} \tag{22}$$

where equation (19b) is used in next-to-the-last equality, and the last equality is the definition of the integral I_0.

One then inserts (21) in (22) to obtain the magnitude of the driving force in the modified system,

$$F_0 = v_0/2I_0, \tag{23}$$

where the integral I_0 (mostly) needs to be calculated numerically. Equation (19a) then becomes

$$F_1' = \frac{v_0/2I_0}{1 + \mathrm{i}\omega M Y(\omega)}. \tag{24}$$

The time history of this force can be found by means of the inverse Fourier transform, $f_1'(t) = \mathcal{F}_t^{-1}\{F_1'\}$, implemented numerically as a fast digital inverse transform. The moment in time of the first zero crossing of the force is obtained then as

$$t_{cut} = \min\{t | t > 0,\ f_1'(t) = 0\}. \tag{25}$$

The actual, interrupted, excitation impact force then is

$$f_1(t) = f_1'(t)\theta(t_{cut} - t), \tag{26}$$

the corresponding force spectrum being found by means of a Fourier transform $F_1 = \mathcal{F}_t\{f_1(t)\}$, implemented numerically as a fast digital transform. The Fourier series components of (4) are $F_n = F_1(nf_r)f_r$, where $f_r = 1/T_r$ is the repetition frequency of the tapping machine.

4.2. The driving-point mobility

In the lumped system description presented in section 3, which made use of frequency-independent components, both the stiffness and the resistance were important for the solution. For a general mobility, this implies that both the real and the imaginary part of the mobility are important.

For an infinite homogenous plate, the imaginary part of the mobility, or the finite stiffness, can only be due to local effects. In section 3, the stiffness was chosen to be the stiffness due to deformation near the impact zone on a semi-infinite elastic solid, the Bossinesq expression (16). It would be more realistic to determine the local stiffness of a plate of finite thickness, i.e. to treat the plate as an elastic continuum. The force excites the plate asymmetrically on its upper surface. Thus, the excitation force produces a complicated displacement field under and near the point of excitation.

However, the description of the elastic continuum has too high a level of complexity to be appropriate for the entire system, including the reinforcing beams, for example. To this end, it is better to use thin plate theory, assuming plane sections to remain plane in the plate, which implies the excitation force to be constrained to produce a uniform displacement field in the thickness direction. Thus, no local deformation can be attained in terms of thin plate theory.

A heuristic description of the driving-point mobility could be to combine the mobility as determined for the global system, Y_G, with the mobility as determined for the detailed description near the excitation point, Y_L. Note that both Y_G and Y_L are in general complex. The parts of the mobilities that overlap need to be subtracted, i.e. the mobility of an infinitely thin plate. The total mobility is expressed as a correction of the global mobility,

$$Y = Y_G + \triangle Y,\ \triangle Y = Y_L - 1/8\sqrt{m'' B}, \tag{27}$$

where m'' is the mass per unit area and B is the bending stiffness of the excited plate. This is quite an elaborate description of the driving-point mobility. The mobilities Y_L and Y_G need to be determined then.

One can also use measured mobilities as an alternative to the theoretically derived mobilities, provided the frequency resolution is sufficiently high.

4.3. Local effects on the mobility

The mobility Y_L due to local effects needs to be determined, the global parts of the system being excluded. The mobility of a plate of finite thickness and infinite extent excited on its upper surface by an indenter, is described in the literature. The indenter is assumed to be circular, weightless and stiff as compared with the plate, and to be small as compared with the wavelengths of the bending and quasi-longitudinal waves of the plate. A rigid indenter, such as the case of a metal hammer acting on a wooden or a gypsum plate, can be assumed to provide a better approximation of the actual situation than a soft indenter would. Use of a rigid indenter is also more reasonable than use of a soft one (assuming the pressure distribution to be uniform), since it allows the pressure distribution under the indenter to change as the frequency increases.

In all analyses describing the motion of 'thin' structures, such as in the Kirchoff and the Mindlin theories, it is assumed that the two sides of the structure have exactly the same displacement at each point. This is an approximation, and both additional weakness and inertia effects can occur. Thus, simplified 'thin' theories are not sufficient for the case at hand.

More detailed three-dimensional analyses have been carried out, such as by Ljunggren [14] for a rigid indenter and by Heckl [15] for a soft indenter. Petersson and Heckl [11] have investigated the influence of different choices of pressure distribution. The boundary value problem is simpler mathematically in the case of a soft indenter than of a rigid one. Therefore, by assuming a pressure distribution under the indenter, Ljunggren [14], and Petersson and Heckl [11] (when dealing with a rigid indenter) avoided the problems a rigid indenter involves. The pressure distribution taken was that of a rigid indenter statically loading an elastic semi-infinity. Since there is no guarantee that this assumption actually results in a uniform displacement under the indenter, such a case can be designated as quasi-rigid.

In a paper by the authors [16], the pressure distribution at the interface between the indenter and the plate was determined by use of a variational formulation. The expressions obtained are approximations, although the choice of

these is an optimal one. The mobility described in [16] is written as

$$Y_L = \frac{1}{2\pi R^2}\frac{I_a I_c - I_b^2}{I_c - I_b + I_a/4} \tag{28}$$

where

$$I_a = \int_0^\infty \frac{\sin^2(Rk_r)}{k_r} A(k_r)\mathrm{d}k_r, \tag{29}$$

$$I_b = \int_0^\infty \frac{\mathrm{J}_1(k_r R)\sin(Rk_r)}{k_r} A(k_r)\mathrm{d}k_r, \tag{30}$$

$$I_c = \int_0^\infty \frac{\mathrm{J}_1^2(k_r R)}{k_r} A(k_r)\mathrm{d}k_r, \tag{31}$$

and where $A(k_r)$ is the admittance, used in all the references [11, 14, 15, 16].

It should be pointed out that only the imaginary part of Y_L can be said to be due to local deformation, the real part being due to the rest of the system as well, and it is in a broad frequency range close to $1/8\sqrt{m'' B}$.

4.4. Global effects on the mobility

The mobility Y_G due to global considerations needs to be determined, local effects near the excitation zone being excluded. Both the real and the imaginary parts of the driving-point mobility of the floor structure may be due to global effects. An infinite thin plate has a real mobility, whereas in a finite plate, if no damping is included, the mobility is entirely imaginary. Thus, an infinite plate has only a resistance part in the mobility, whereas a finite plate has only stiffness and mass parts in the mobility. In lightweight floors consisting of plates reinforced by beams, the mobility has an imaginary part, also in the case of infinite systems. In [2], a typical lightweight floor system is described by use of a spatial Fourier transform method. The driving-point mobility due to global effects can be derived using the same strategy.

Assume that the transformed displacement field is found in a way similar to that presented in [2]. The driving-point displacement can be found then by means of a double inverse Fourier transform in spatial coordinates,

$$w(x_0, y_0) = \frac{1}{4\pi}\iint_{-\infty}^{\infty} \tilde{w}(\alpha,\beta)\mathrm{e}^{-\mathrm{i}(x_0\alpha + y_0\beta)}\mathrm{d}\alpha\mathrm{d}\beta, \tag{32}$$

where w is the displacement field of the excited plate, $\tilde{w}$ is the spatially transformed displacement field, x_0 and y_0 are the coordinates of excitation, and α and β are the transform wavenumbers. An account of how to simplify and reduce the integrals in (32) to be suited for numerical integration is presented in the Appendix. A simplified floor system is also described there.

The driving-point mobility due to global considerations is defined as

$$Y_G = v(x_0, y_0)/F_1 = \mathrm{i}\omega w(x_0, y_0)/F_1 \tag{33}$$

How the driving-point mobility is determined is not crucial, however, for the methods in section 4.1. One can use modal sums, FEM or any other deterministic method, as long as the frequency resolution is sufficiently high.

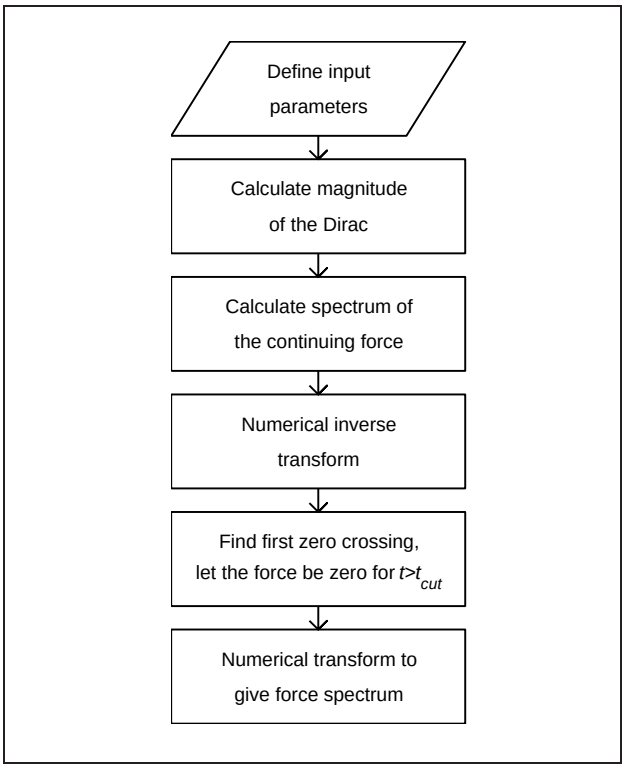

Figure 9. Flow chart for calculation of the force spectrum.

5. Numerical evaluation and programming

Since the impact force description of the general driving-point mobility is not given in the form of a closed expression, program coding is an important part of describing the excitation. Certain important aspects of the program developed will be taken up and be shown in a flowchart (Figure 9).

The program starts by defining the input parameters, including that the driving-point mobility Y is to be determined. Equations (28–31) are used for the local part of the mobility. The global part of the mobility can be integrated from equations (32–33), see also the Appendix. In the numerical example to be taken up, an adaptive and recursive Newton-Cotes eight-panel integration scheme, the Matlab function `quad8` [17], was used in the numerical evaluation. In order to speed up the calculations, a frequency resolution of 10 Hz was employed, and the frequency range being 10 Hz to 6000 Hz. The numerical 'signal theoretic' methods described in section 4.1 are in need of a better frequency resolution and of a broader frequency range, as will soon be evident. The narrower frequency range is achieved using a spline interpolation, and the extended frequency range is achieved by using the asymptotic mobilities of an infinite plate for excitation positions between beams, and of an infinite beam for excitation positions at the beams.

The magnitude of the Dirac shown in Figure 8 c needs to be calculated then, by use of (22) and (23). The spectrum of the continuing force is calculated then from (24) and numerically inverse transformed by use of the IFFT algorithm. It is important that the frequency resolution is sufficient to describe the pulse peak and detect the first zero-crossing correctly.

As an example, consider the lumped model with $R = 2 \cdot 10^3$; and $K = 2 \cdot 10^7$, use of (14) showing that $t_{cut} = 8.112 \cdot 10^{-4}$ s. An appropriate time resolution might then be > 20 points for describing the force pulse. Thus, the time resolution should be $\triangle t < 4.06 \cdot 10^{-5}$ s, giving an upper frequency limit of $f_{nyq} > 12.3 \cdot 10^3$ Hz (the Nyquist frequency). If a frequency resolution of $\triangle f = 2$ Hz is employed, an FFT/IFFT of 16384 points is needed.

In the numerical example to be presented, the resolution data chosen were; $\triangle t = 8.33 \cdot 10^{-6}$ s, $\triangle f = 3.66$ Hz and $f_{nyq} = 60 \cdot 10^3$ Hz, a 16384-points FFT/IFFT being employed. Since the impact noise is often only of interest up to 5000 Hz a low-pass filter of $10 \cdot 10^3$ Hz was used, to prevent high-frequency terms from influencing the force spectrum.

The first zero-crossing needs to be found then, so that the actual, interrupted impact force was determined from (26). The zero-crossing was found by examining the change of sign. The exact position could not be determined since the time resolution is fixed. The force spectrum was calculated then by use of the fast digital Fourier transform FFT, the same resolution data as before being employed.

Due to the material models and numerical procedures there will be some causality problems in the procedure. If the force is non-zero before and at the time of impact $t = 0$ it clearly violating the causality rules. This not only produces a wrong result, but also complicates the numerical treatment since sometimes more than one zero crossing may need to be found. However, when the time and frequency resolution are good and the damping is slight, problems of this sort are held to a minimum, its being assumed in such cases that the errors involved can be disregarded.

6. Numerical results and discussion

A numerical example will be given to illustrate the excitation force description when a frequency dependent driving-point mobility is employed. One plate reinforced by one set of periodically spaced beams, as described in the Appendix, is used instead of the complete floor structure, so as to simplify the calculations.

The following data were used in the numerical calculations: distance between beams $l = 0.6$ m, modulus of the plates $E_p/(1-\mu^2) = 7.2 \cdot 10^9$ Pa, Young's modulus for the framing beams $E_f = 9.8 \cdot 10^9$ Pa, density of the beams and plates $\rho_p = \rho_f = 500\ \mathrm{kg/m^3}$, thickness of the plates $h = 22 \cdot 10^{-3}$ m, and material damping $\eta = 0.03$. The beams are 0.220 m in height and 0.067 m in width.

The magnitude of the driving-point mobility is shown in Figure 10, calculated there for 15 positions. These

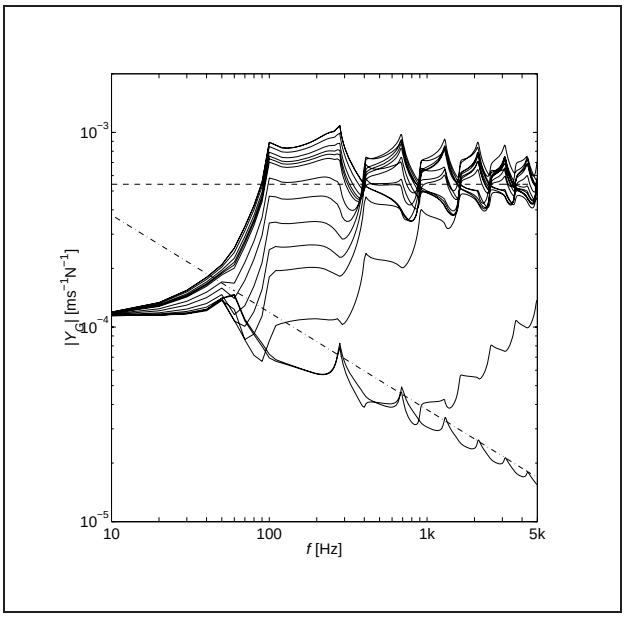

Figure 10. Global driving-point mobility at 15 positions, solid line (—). Driving-point mobility for an infinite plane, dashed line (- - -). Driving-point mobility for an infinite beam, dashed-dotted line (- · -).

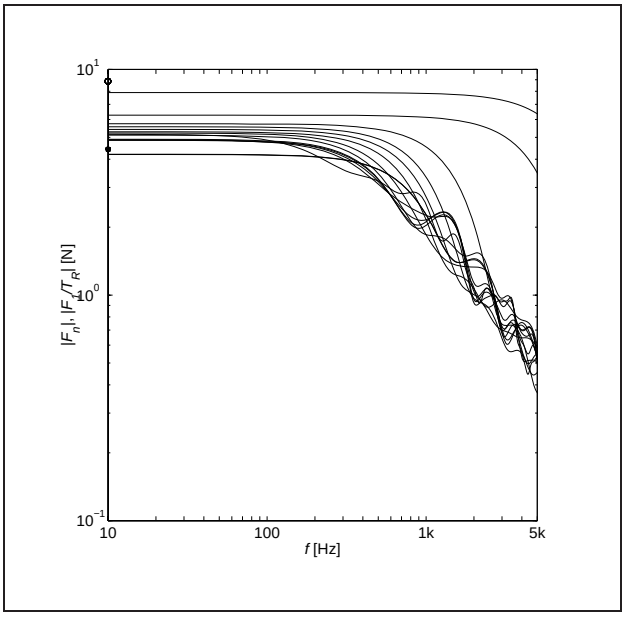

Figure 11. Force spectrum, calculated according to sections 4 and 5. Mobility is taken as the global one, see section 4.4, no local weakness are present.

are the global mobilities. The excitation co-ordinates are $x_0 = \{0\ \ 0.012\ \ 0.053\ 0.084\ \ 0.101\ \ 0.122\ 0.150\ \ 0.175\ 0.205\ 0.213\ 0.220\ 0.232\ 0.255\ 0.291\ 0.3\}$ m (chosen randomly) and $y_0 = 0$ m. These mobilities are used as input data in calculating the impact force. The asymptotic mobilities for an infinite plate $(\cdots)$ and for an infinite beam (-·-) are also shown in the figure.

The force spectrum resulting from the mobilities contained in Figure 10, without consideration of local effects, is shown in Figure 11. The points of excitation are clearly

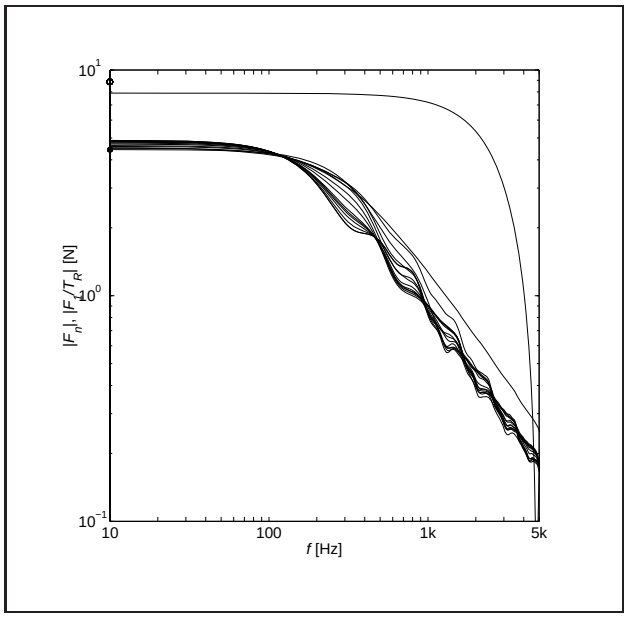

Figure 12. Force spectrum, calculated according to 4 and 5. Mobility taken as the global one in section 4.4, but with local weakness added in accordance with section 4.3.

important, since these differ both in the low-frequency asymptote and at the cutoff frequency. The extremes of the low-frequency asymptotes are indicated by one star ($*$) and one circle ($\circ$) on the ordinata. One of the curves fall outside the extremes, implying the numerical procedures to not be perfect. The errors, however, are minor, the important features being clearly illustrated. It should be pointed out that for this case there are no problems concerning causality.

In Figure 12 the local mobility has been added to the global mobility, in accordance with equation (27), the force spectrum being calculated then. Local effects are also important; the corresponding excitation points in Figures 11 and 12 differ both in the asymptote and in the cutoff frequency. The cutoff frequency and the low-frequency asymptote are consisting less in Figure 12.

7. Summary and conclusions

Findings concerning the excitation force achieved by the ISO tapping machine, as reported in the literature, have been summarised and reconsidered. A two-parameter lumped model of impact developed by Lindblad [5], was analysed. The model can only deal with frequency-independent parameters. Low-frequency asymptotes and cutoff frequencies were derived. The low-frequency asymptotes were found to have a span of 6 dB. The lumped parameters were taken as the local stiffness and the driving-point mobility of an infinite plate. On the basis of a numerical parametric study, it was concluded that increasing the stiffness gives a lower low-frequency asymptote and a higher cutoff frequency, and that increasing the resistance gives a higher low-frequency asymptote, as well as an unchanged undamped cutoff frequency and a lower actual cutoff frequency.

A description of impact force applicable to general, frequency-dependent impedances and mobilities was derived. The general force description was implemented by means of numerical integration and FFT. The mobilities may be due to local effects, to the use of thick plate theory, and/or global effects, obtained using spatial Fourier transform methods and numerical integration. From a numerical example it was concluded that both the local and the global effects are important in determining the excitation force of the ISO tapping machine on a non-homogenous lightweight floor. In order to adequately describe what occurs, the global and the local driving-point mobility has to be used and combined. The results also indicate how important it is to use an accurate and detailed system description in order to predict the impact force spectrum appropriate. The force spectrum needs to be determined on the basis of the entire driving-point mobility, that is both the real and the imaginary parts.

Appendix

The driving-point mobility is needed for determining the force spectrum of the tapping machine. A simplified system for performing the calculations is considered, one taking account of the upper plate and the beams. Moreover, the fluid reaction is not taken into account. The simplification and the reductions of the number of integrals to be evaluated are inspired by Mace [18, 19]. The transformed displacement used in this system, discussed by Evseev [20] and Mace [21] and also in [2], can be written as

$$\begin{aligned}\tilde{w}(\alpha,\beta) &= \frac{F_R \mathrm{e}^{\mathrm{i}(\alpha x_0+\beta y_0)}}{S(\alpha,\beta)} \\ &\quad - \frac{P_a(\alpha,\beta)G(\beta)/l}{S(\alpha,\beta)(1+P_b(\alpha,\beta)G(\beta)/l)},\end{aligned} \tag{A1}$$

where

$$S(\alpha,\beta) = D\big((\alpha^2+\beta^2)^2-\kappa^4\big), \tag{A2}$$

$$G(\beta) = E_f I_f \beta^4 - \rho_f A_f \omega^2, \tag{A3}$$

are the transformed plate and beam operators, respectively, D is the bending stiffness of the plate, κ the bending wave number, $E_f I_f$ the bending stiffness of the beam and $\rho_f A_f$ the mass per unit length of the beam. The two help functions P_a and P_b are

$$P_a(\alpha,\beta) = \frac{F_R \mathrm{e}^{\mathrm{i}\beta y_0}}{D} \sum_{n=-\infty}^{\infty} \frac{\mathrm{e}^{\mathrm{i}(\alpha-en)x_0}}{\big((\alpha-en)^2+\beta^2\big)^2-\kappa^4}, \tag{A4}$$

$$P_b(\alpha,\beta) = \frac{1}{D} \sum_{n=-\infty}^{\infty} \frac{1}{\big((\alpha-en)^2+\beta^2\big)^2-\kappa^4}, \tag{A5}$$

where, as before, $e = 2\pi/l$ and κ is the bending wave number. The fluid reaction is not included in equations (A2–A5) .

The inverse transform $w(x,y) = \mathcal{F}_{x,y}^{-1}\{\tilde{w}(\alpha,\beta)\}$ is defined in [2], equation (2 b). The half-way transform, transformed in the $y-\beta$ direction or inverse transformed in the $x-\alpha$ direction, is denoted $\breve{w}(x,\beta) = \mathcal{F}_x^{-1}\{\tilde{w}(\alpha,\beta)\} = \mathcal{F}_y\{w(x,y)\}$.

Define a function Λ for the sums in (A4–A5),

$$\Lambda(\alpha,\beta;x_0) = \sum_{n=-\infty}^{\infty} \frac{\mathrm{e}^{\mathrm{i}(\alpha-en)x_0}}{\big((\alpha-en)^2+\beta^2\big)^2-\kappa^4}. \quad \text{(A6)}$$

Thus, equations (A4) and (A5) can be expressed in terms of Λ,

$$\begin{aligned} P_a(\alpha,\beta) &= F_R\mathrm{e}^{\mathrm{i}\beta y_0}\Lambda(\alpha,\beta;x_0)/D, \\ P_b(\alpha,\beta) &= \Lambda(\alpha,\beta;0)/D. \end{aligned}$$

The function Λ can be given explicitly using the Poisson's sum formula, contour integration and a geometric series expression, a method described in Mace [18, 19]. After considerable manipulations, equation (A6) can be expressed as

$$\begin{aligned} &-\frac{4\kappa^2}{l}\Lambda(\alpha,\beta;x_0) \\ &= \frac{\mathrm{i}\mathrm{e}^{-ix_0q_-}/q_-}{1-\mathrm{e}^{-\mathrm{i}l(\alpha+q_-)}} - \frac{\mathrm{i}\mathrm{e}^{ix_0q_-}/q_-}{1-\mathrm{e}^{-\mathrm{i}l(\alpha-q_-)}} \\ &+ \frac{\mathrm{e}^{-x_0q_+}/q_+}{1-\mathrm{e}^{-l(\mathrm{i}\alpha+q_+)}} - \frac{\mathrm{e}^{x_0q_+}/q_+}{1-\mathrm{e}^{-l(\mathrm{i}\alpha-q_+)}} \end{aligned} \quad \text{(A7)}$$

for $0 < x_0 < l$, and where $q_+ = \sqrt{\kappa^2+\beta^2}$ and $q_- = \sqrt{\kappa^2-\beta^2}$. For other positions of x_0, the periodicity of the structure can be used to translate the co-ordinates so that the inequality is fulfilled. However, the sum in (A6) converges rapidly (due to the fourth-order expression in the nominator) making it possible to use a truncated sum instead of the explicit expression (A7). When the fluid reaction is included, a truncated sum needs to be employed.

The integrals in the inverse transform is now to be evaluated,

$$\begin{aligned} \breve{w}(x,\beta) &= \frac{1}{2\pi}\int_{-\infty}^{\infty} \frac{F_R\mathrm{e}^{\mathrm{i}(\alpha x_0+\beta y_0)}}{S(\alpha,\beta)}\mathrm{e}^{-\mathrm{i}\alpha x}\mathrm{d}\alpha \\ &- \frac{1}{2\pi}\int_{-\infty}^{\infty} \frac{P_a(\alpha,\beta)G(\beta)l^{-1}\mathrm{e}^{-\mathrm{i}\alpha x}}{S(\alpha,\beta)\big(1+P_b(\alpha,\beta)G(\beta)/l\big)}\mathrm{d}\alpha \\ &= I_1 - I_2, \end{aligned} \quad \text{(A8)}$$

where the integrals I_1 and I_2 are defined. The second integral in (A8) is

$$\begin{aligned} I_2 &= \frac{G(\beta)F_R\mathrm{e}^{\mathrm{i}\beta y_0}}{2\pi lD} \\ &\times \int_{-\infty}^{\infty} \frac{\Lambda(\alpha,\beta;x_0)\mathrm{e}^{-\mathrm{i}\alpha x}\mathrm{d}\alpha}{S(\alpha,\beta)\big(1+\Lambda(\alpha,\beta;0)G(\beta)/lD\big)} \end{aligned} \quad \text{(A9)}$$

In order to simplify the integration, subdivide the infinite integral I_2 into an infinite sum of finite integrals,

$$\int_{-\infty}^{\infty}\cdot\ \mathrm{d}\alpha = \sum_{n=-\infty}^{\infty}\int_{(2n-1)\pi/l}^{(2n+1)\pi/l}\cdot\ \mathrm{d}\alpha \quad \text{(A10)}$$

Making use of the periodic behaviour of the infinite sums yields

$$\Lambda(\alpha,\beta;x_0) = \Lambda(\alpha+2n\pi/l,\beta;x_0).$$

A variable substitution $\alpha' = \alpha - 2n\pi/l$ and a change of order between the sum and the integral, allow (A9) to be written as

$$\begin{aligned} I_2 &= \frac{G(\beta)F_R\mathrm{e}^{\mathrm{i}\beta y_0}}{2\pi lD} \\ &\times \int_{-\pi/l}^{\pi/l} \frac{\displaystyle\sum_{n=-\infty}^{\infty} \frac{\mathrm{e}^{-\mathrm{i}(\alpha+en)x}}{S(\alpha'+en,\beta)}\Lambda(\alpha',\beta;x_0)\mathrm{d}\alpha'}{1+\Lambda(\alpha',\beta;0)G(\beta)/lD} \end{aligned} \quad \text{(A11)}$$

The sum in (A11) is identified as

$$\sum_{n=-\infty}^{\infty} \frac{\mathrm{e}^{-\mathrm{i}(\alpha+en)x}}{S(\alpha'+en,\beta)} = \Lambda(-\alpha',\beta;x)/D.$$

Thus, I_2 becomes a finite integral,

$$\begin{aligned} I_2 &= \frac{G(\beta)F_R\mathrm{e}^{\mathrm{i}\beta y_0}}{2\pi lD} \\ &\times \int_{-\pi/l}^{\pi/l} \frac{\Lambda(-\alpha',\beta;x)\Lambda(\alpha',\beta;x_0)\mathrm{d}\alpha'}{1+\Lambda(\alpha',\beta;0)G(\beta)/lD} \end{aligned} \quad \text{(A12)}$$

Since the driving-point mobility is to be evaluated, $x = x_0$. Utilising this and the fact that Λ is symmetric in a if $x = 0$, $\Lambda(\alpha,\beta;0) = \Lambda(-\alpha,\beta;0)$, can be used to reduce the integral to

$$\begin{aligned} I_2 &= \frac{G(\beta)F_R\mathrm{e}^{\mathrm{i}\beta y_0}}{\pi lD} \\ &\times \int_{0}^{\pi/l} \frac{\Lambda(-\alpha',\beta;x)\Lambda(\alpha',\beta;x_0)\mathrm{d}\alpha'}{1+\Lambda(\alpha',\beta;0)G(\beta)/lD} \end{aligned} \quad \text{(A13)}$$

The first integral in (A8) is

$$I_1 = \frac{F_R\mathrm{e}^{\mathrm{i}\beta y_0}}{2\pi}\int_{-\infty}^{\infty}\frac{\mathrm{d}\alpha}{S(\alpha,\beta)} \quad \text{(A14)}$$

After use of (A10), variable substitution and change of order between the sum and the integral and identifying Λ, I_1 can be written as a finite integral. The negative side can be reduced using the symmetry of Λ in α, yielding

$$I_1 = \frac{F_R\mathrm{e}^{\mathrm{i}\beta y_0}}{\pi}\int_{0}^{\pi/l}\Lambda(\alpha',\beta,0)\mathrm{d}\alpha' \quad \text{(A15)}$$

The integral in the β-direction is now to be evaluated. The complete inverse transform is written as

$$\begin{aligned} w(x_0,y_0) &= \frac{1}{2\pi}\int_{-\infty}^{\infty} I_1(\beta)\mathrm{e}^{-\mathrm{i}\beta y_0}\,\mathrm{d}\beta \\ &- \frac{1}{2\pi}\int_{-\infty}^{\infty} I_2(\beta)\mathrm{e}^{-\mathrm{i}\beta y_0}\,\mathrm{d}\beta = J_1 - J_2. \end{aligned} \quad \text{(A16)}$$

where the integrals J_1 and J_2 are defined. The second term is

$$J_2 = \frac{F_R}{2\pi^2 lD} \times \int_{-\infty}^{\infty} G(\beta) \int_0^{\pi/l} \frac{\Lambda(-\alpha,\beta;x)\Lambda(\alpha,\beta;x_0)\mathrm{d}\alpha\mathrm{d}\beta}{1+\Lambda(\alpha,\beta;0)G(\beta)/lD}. \quad \text{(A17)}$$

The symmetry of the functions $\Lambda(\alpha,-\beta;x_0) = \Lambda(\alpha,\beta;x_0)$ and $G(-\beta) = G(\beta)$ can be used to reduce the integral to

$$J_2 = \frac{F_R}{\pi^2 lD} \times \int_0^{\infty} G(\beta) \int_0^{\pi/l} \frac{\Lambda(-\alpha,\beta;x)\Lambda(\alpha,\beta;x_0)\mathrm{d}\alpha\mathrm{d}\beta}{1+\Lambda(\alpha,\beta;0)G(\beta)/lD}. \quad \text{(A18)}$$

The first integral J_1 can be shown to be

$$J_1 = \frac{F_R}{4\pi^2} \iint_{-\infty}^{\infty} S^{-1}\mathrm{d}\alpha\mathrm{d}\beta = \frac{F_R}{\mathrm{i}\omega 8\sqrt{m''D}}.$$

It is better numerically, however, to evaluate this integral in the same way as J_2. Thus, if the symmetry is used

$$J_1 = \frac{F_R}{\pi^2} \int_0^{\infty} \int_0^{\pi/l} \Lambda(\alpha,\beta;0)\mathrm{d}\alpha\mathrm{d}\beta. \quad \text{(A19)}$$

Summing up (A18) and (A19), the inverse transform (A16) can now be written as

$$w(x_0,y_0) = \frac{F_R}{\pi^2} \int_0^{\infty} \int_0^{\pi/l} \Lambda(\alpha,\beta;0) - \frac{\Lambda(\alpha,\beta;x_0)\Lambda(-\alpha,\beta;x_0)G(\beta)}{lD+\Lambda(\alpha,\beta;0)G(\beta)}\mathrm{d}\alpha\mathrm{d}\beta, \quad \text{(A20)}$$

where (A20) is to be evaluated numerically. The driving-point mobility is found by using the results presented in sections 4.2 to 4.4.

Acknowledgements

The authors thank their colleagues at the Division of Engineering Acoustics at LTH, Lund University, for the helpful suggestions and criticism they have provided, in particular Dag Holmberg. The financial support provided by Skanska Teknik AB, 'The Building and its Indoor Environment' research school at Lund university (the KK-foundation) and SBUF is also thankfully acknowledged.

References

[1] ISO 140-6: – Acoustics – Measurement of sound insulation in buildings and building elements – part 6: Laboratory measurments of impact sound insulation of floors.

[2] J. Brunskog, P. Hammer: Prediction model for the impact sound level of lightweight floors. Acta Acustica / Acustica **89** (2003) 309–321.

[3] J. Brunskog, P. Hammer: Prediction models of impact sound insulation on timber floor structures; a literature survay. Journal of Building Acoustics **7** (2000) 89–112.

[4] L. Cremer, M. Heckl, E. E. Ungar: Structure-borne sound. Springer-Verlag, Berlin, 1988.

[5] S. Lindblad: Impact sound characteristics of resilient floor coverings. a study on linear and nonlinear dissipative compliance. Dissertation. Division of Building Technology, Lund Institute of Technology, Lund, Sweden, 1968.

[6] Vér: Impact noise isolation of composite floors. Journal of the Acoustical Society of America **50** (1971) 1043–1050.

[7] E. Gerretsen: Calculation of airborne and impact sound insulation between dwellings. Applied Acoustics **19** (1986) 245–264.

[8] W. Scholl, W. Maysenhölder: Impact sound insulation of timber floors: Interaction between source, floor coverings and load bearing floor. J. Building Acoustics **6** (1999) 43–61.

[9] R. Hall: The standard impact test and thin floating floor constructions. Institute of Acoustics. Proceedings, Volume 22 Pt 2, 77A St Peters's Street, St Albans, Herts AL1 3BN, UK, 2000, 43–50.

[10] S. Timoshenko: Theory of elasticity. McGraw-Hill Book Company, New York and London, 1939.

[11] B. A. T. Petersson, M. Heckl: Concentrated excitaion of structures. Journal of Sound and Vibration **196** (1996) 295–321.

[12] S. Gudmundsson: Sound insulation improvment of floating floors. A study of parameters. TVBA–3017. Dissertation. Building Acoustics, LTH, Lund University, Lund, Sweden, 1984.

[13] C. L. Morfey: Dictionary of acoustics. Academic press, 2001.

[14] S. Ljunggren: Generation of waves in an elastic plate by a vertical force and by a moment in the vertical plane. Journal of Sound and Vibration **90** (1983) 559–584.

[15] M. Heckl: Körperschallübertragung bei homogenen platten beliebiger dicke. Acustica **49** (1981) 183–191.

[16] J. Brunskog, P. Hammer: Rigid indenter excitation of plates. Acta Acustica / Acustica (accepted).

[17] MATLAB Reference guide. The MathWorks, Inc., 1992.

[18] B. R. Mace: Periodically stiffened fluid-loaded plates, I: Responce to convected harmonic pressure and free wave propagation. Journal of Sound and Vibration **73** (1980) 473–486.

[19] B. R. Mace: Periodically stiffened fluid-loaded plates, II: Responce to line and point forces. Journal of Sound and Vibration **73** (1980) 487–504.

[20] V. N. Evseev: Sound radiaton from an infinite plate with periodic inhomogeneities. Soviet physics – Acoustics **19** (1973) 345–351.

[21] B. R. Mace: Sound radiate from a plate reinforecd by two sets of parallel stiffeners. Journal of Sound and Vibration **71** (1980) 435–441.